Supporting Information

For

Solvent-dependent SCO behavior of dinuclear iron(II) complexes with a 1,3,4-thiadiazole bridging ligand

Christian F. Herold, Sergii I. Shylin, Eva Rentschler

Institute of Inorganic and Analytical Chemistry, Johannes Gutenberg University, Mainz, Germany

Corresponding Author

E-mail: rentschler@uni-mainz.de

Table of Contents

Experimental Section

Protocol for the desolvation/resolvation of 1·4DMF and 1:

Desolvation:

Single crystals of **1·4DMF** have been desolvated under high vacuum ($5*10^{-2}$ mbar) in a glass oven at 150 °C. The red single crystals of **1·4DMF** lost their crystallinity upon heating under high vacuum and a pale brown powder of **1** was obtained after 10 hours.

Elemental analysis and IR of **1** after dehydration of **1·4DMF** under HV at 150°C:

Anal. Calcd (%) $C_{32}H_{36}B_4F_{16}Fe_2N_{12}S_2$: C, 34.57; H, 3.26; N, 15.12; S, 5.77. Found: C, 34.46; H, 3.21; N, 15.11; S, 5.90.

IR (cm^{-1}): 3431(w), 3103(w), 2905(w), 1631(w), 1610(s), 1572(s), 1487(s), 1442(m), 1385(m), 1350(m), 1296(m), 1083(w), 1057(w), 898(m), 771(s), 533(s), 522(s).

Resolvation of **1** with DMF:

The resolvation of **1** with DMF was performed in a glove box under a dry nitrogen atmosphere.

A sample of **1** in a sample vial was placed in a larger vial with dry DMF and has been removed after 8-9 hours. The color of the pale brown powder changed during the resolvation with DMF to very dark brown.

Preparation of 1·1.5H_2O:

A sample of **1·1.5H_2O** was obtained by vapor diffusion of water into a powder sample of **1**. A sample vial with **1** has been placed in a larger vial with water and this has been flushed with argon. The sample vial has been removed after one day. The previously light brown powder changed the color to a very dark brown.

Anal. Calcd (%) $C_{33}H_{38}B_4F_{16}Fe_2N_{12}S_2O_{1.5}$: C, 33.75; H, 3.45; N, 14.76; S, 5.63. Found: C, 33.84; H, 3.46; N, 14.79; S, 5.55.

IR (cm^{-1}): 3422(w), 3145(w), 2930(w), 1636(w), 1439(m), 1385(s), 1123(m), 1084(m), 1034(s), 764(s), 534(s), 523(s).

Crystallographic Data

Table S1. Crystallographic parameters for compounds **1·4DMF** and **2·4DMF**.

	1·4DMF	**2·4DMF**
formula	$C_{44}H_{64}B_4F_{16}Fe_2N_{16}O_4S_2$	$C_{44}H_{64}Cl_4Fe_2N_{16}O_{20}S_2$
formula weight	1404.17	1456.73
crystal system	monoclinic	monoclinic
space group	$P2_1$	$P2_1$
a /Å	11.2504(7)	11.2852(13)
b /Å	23.3121(17)	23.6660(3)
c /Å	11.3825(6)	11.4497(13)
α /°	90	90
β /°	93.733(2)	93.887(2)
γ /°	90	90
V /Å^3	2979.0(3)	3050.9(6)
Z	2	2
T /K	173	193
$\rho_{calcd.}$ [g/cm^3]	1.565	1.584
μ [mm^{-1}]	0.664	0.804
R(int)	0.0546	0.0303
S	0.956	1.037
*R*1 (I > 2σ(I))	0.0369	0.0390
*wR*2 (all data)	0.0844	0.0933
av. Fe-N /Å [a]	1.987/1.990	1.989/1.992
Σ /° [a], [b]	59.13/59.66	58.71/59.81

[a] Fe1/Fe2, [b] octahedral distortion parameter Σ (sum of the deviation from 90° of the 12 *cis* N-Fe-N angles in the FeN_6 coordination sphere)

Table S2. Selected bond lengths (Å) and angles (°) for compound **1·4DMF**.

Fe-N bond lengths		N-Fe-N angles	
Fe1- N1	1.935(2)	N1-Fe1-N5	83.00(10)
Fe1-N5	2.024(2)	N1-Fe1-N6	95.27(14)
Fe1-N6	1.991(3)	N1-Fe1-N7	96.84(10)
Fe1-N7	1.942(2)	N1-Fe1-N11	175.21(14)
Fe1-N11	2.034(3)	N1-Fe1-N12	92.18(14)
Fe1-N12	1.994(3)	N5-Fe1-N11	97.38(11)
		N6-Fe1-N5	81.96(14)
Fe2-N2	1.945(2)	N6-Fe1-N11	89.51(12)
Fe2-N3	2.036(3)	N7-Fe1-N5	176.14(16)
Fe2-N4	2.003(3)	N7-Fe1-N6	94.23(14)
Fe2-N8	1.932(2)	N7-Fe1-N11	83.11(11)
Fe2-N9	2.038(3)	N7-Fe1-N12	92.28(14)
Fe2-N10	1.987(3)	N12-Fe1-N5	91.57(14)
		N12-Fe1-N6	169.46(13)
		N12-Fe1-N11	83.04(12)
		N2-Fe2-N3	82.64(10)
		N2-Fe2-N4	94.99(14)
		N2-Fe2-N9	175.50(15)
		N2-Fe2-N10	93.29(14)
		N4-Fe2-N3	82.59(14)
		N4-Fe2-N9	89.48(13)
		N4-Fe2-N10	169.02(12)
		N8-Fe2-N2	96.81(10)
		N8-Fe2-N3	175.61(15)
		N8-Fe2-N4	93.12(14)
		N8-Fe2-N9	83.45(11)
		N8-Fe2-N10	93.04(14)
		N9-Fe2-N3	97.44(11)
		N10-Fe2-N3	91.34(14)
		N10-Fe2-N9	82.21(13)

Table S3. Selected bond lengths (Å) and angles (°) for compound **2·4DMF**.

Fe-N bond lengths		N-Fe-N angles	
Fe1- N1	1.934(3)	N1-Fe1-N5	82.98(11)
Fe1-N5	2.033(3)	N1-Fe1-N6	94.77(14)
Fe1-N6	1.995(3)	N1-Fe1-N7	96.84(11)
Fe1-N7	1.940(3)	N1-Fe1-N11	175.54(14)
Fe1-N11	2.041(3)	N1-Fe1-N12	92.68(14)
Fe1-N12	1.990(3)	N5-Fe1-N11	97.34(12)
		N6-Fe1-N5	82.14(15)
Fe2-N2	1.942(3)	N6-Fe1-N11	89.68(13)
Fe2-N3	2.041(3)	N7-Fe1-N5	176.04(16)
Fe2-N4	1.994(3)	N7-Fe1-N6	93.94(14)
Fe2-N8	1.935(3)	N7-Fe1-N11	83.15(11)
Fe2-N9	2.040(3)	N7-Fe1-N12	92.60(14)
Fe2-N10	1.997(4)	N12-Fe1-N5	91.36(14)
		N12-Fe1-N6	169.43(13)
		N12-Fe1-N11	82.87(13)
		N2-Fe2-N3	82.74(11)
		N2-Fe2-N4	95.04(15)
		N2-Fe2-N9	175.64(16)
		N2-Fe2-N10	93.06(15)
		N4-Fe2-N3	82.65(15)
		N4-Fe2-N9	89.30(14)
		N4-Fe2-N10	169.13(12)
		N8-Fe2-N2	97.04(11)
		N8-Fe2-N3	175.63(16)
		N8-Fe2-N4	93.03(14)
		N8-Fe2-N9	83.01(12)
		N8-Fe2-N10	93.15(14)
		N9-Fe2-N3	97.54(12)
		N10-Fe2-N3	91.23(14)
		N10-Fe2-N9	82.58(14)

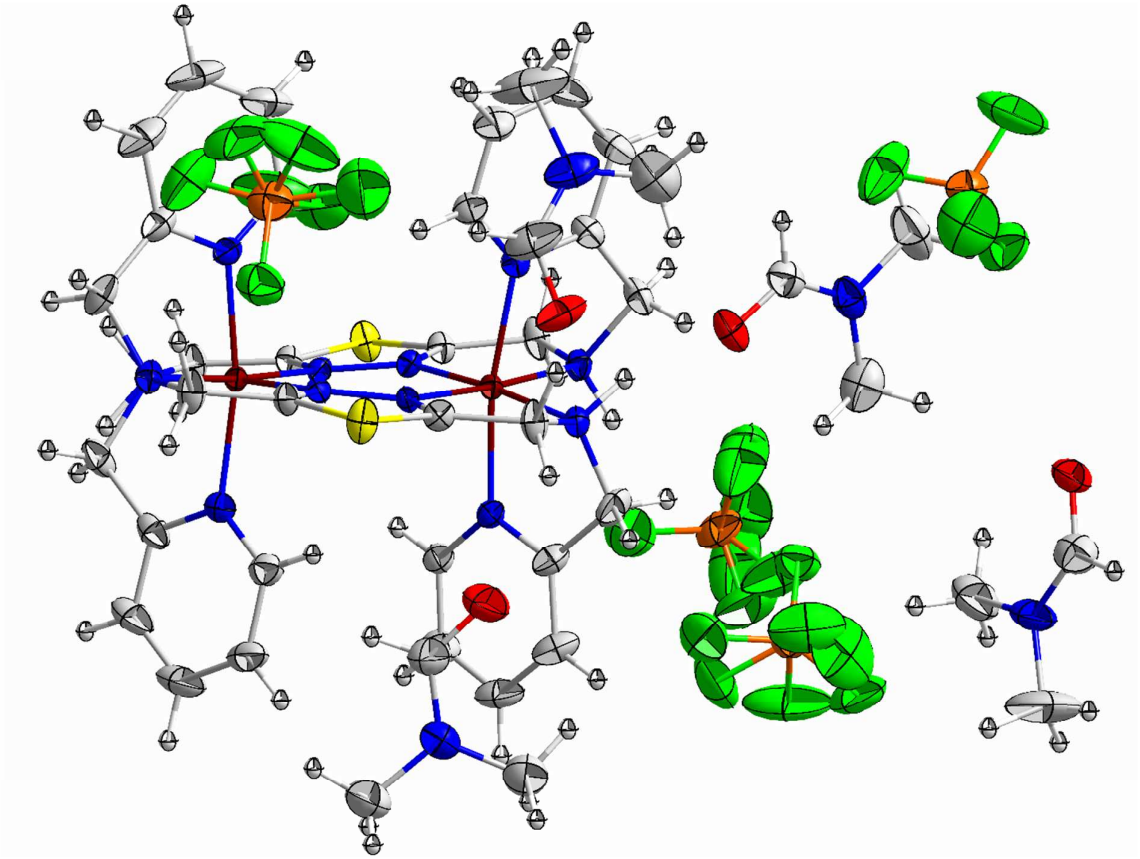

Figure S1: Crystal structure of **1·4DMF** ($[Fe_2(\mu\text{-}L)_2](BF_4)_4$*4DMF).

With thermal ellipsoids drawn at 50% probability level. Colour scheme: dark red – Fe, yellow – S, blue – N, red – O, orange – B, green – F, grey – C, white – H.

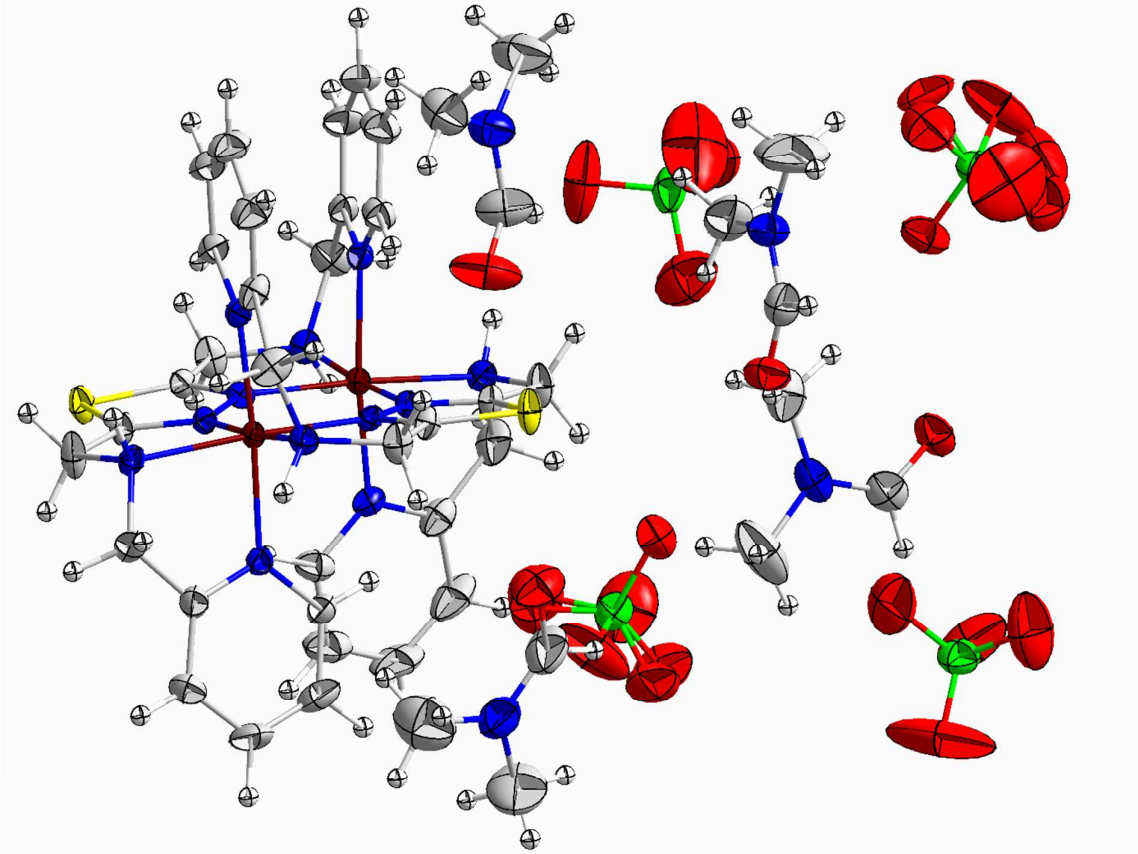

Figure S2: Crystal structure of **2·4DMF** ($[Fe_2(\mu\text{-}L)_2](ClO_4)_4$*4DMF).

With thermal ellipsoids drawn at 50% probability level. Colour scheme: dark red – Fe, yellow – S, blue – N, red – O, green – Cl, grey – C, white – H.

Magnetic Measurements

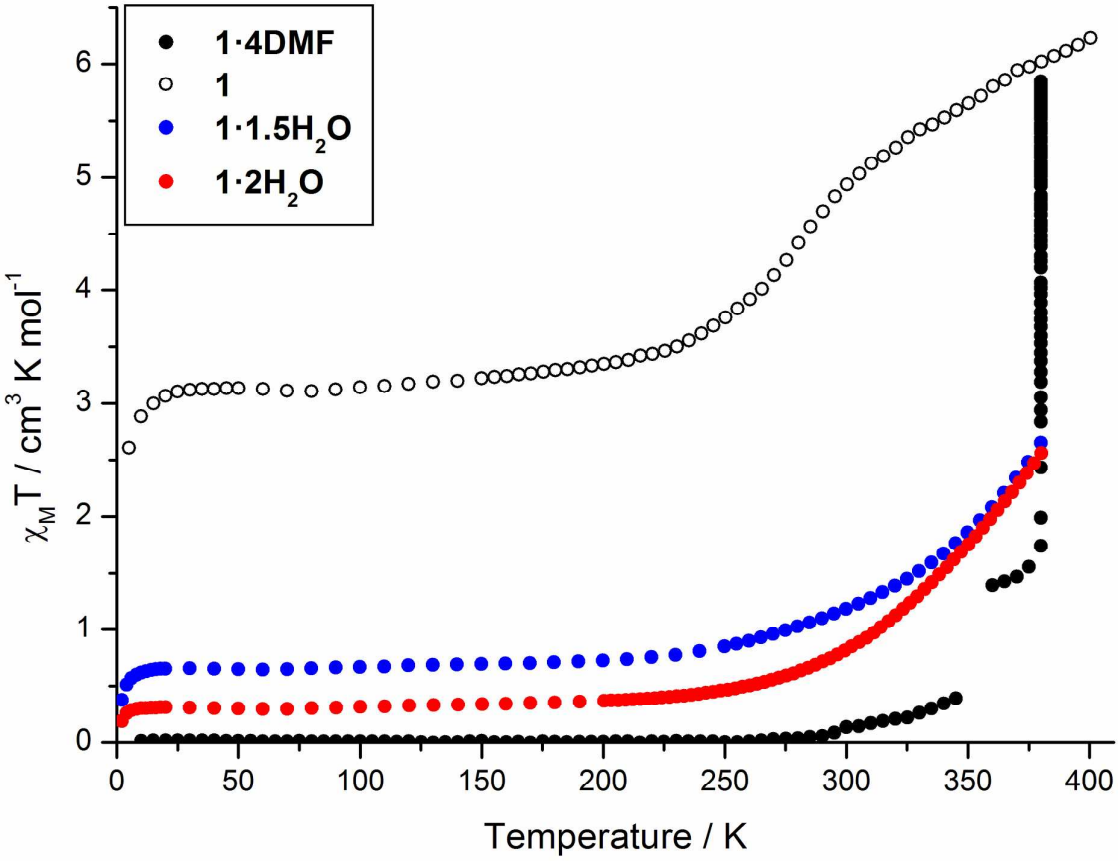

Figure S3: Overlay of the temperature dependence of $\chi_M T$ for compound **1·4DMF** ($[Fe_2(\mu\text{-}L)_2](BF_4)_4$*4DMF), **1** ($[Fe_2(\mu\text{-}L)_2](BF_4)_4$), **1·1.5H$_2$O** ($[Fe_2(\mu\text{-}L)_2](BF_4)_4$*1.5$H_2O$) and **1·2H$_2$O** ($[Fe_2(\mu\text{-}L)_2](BF_4)_4$*2$H_2O$)[1].

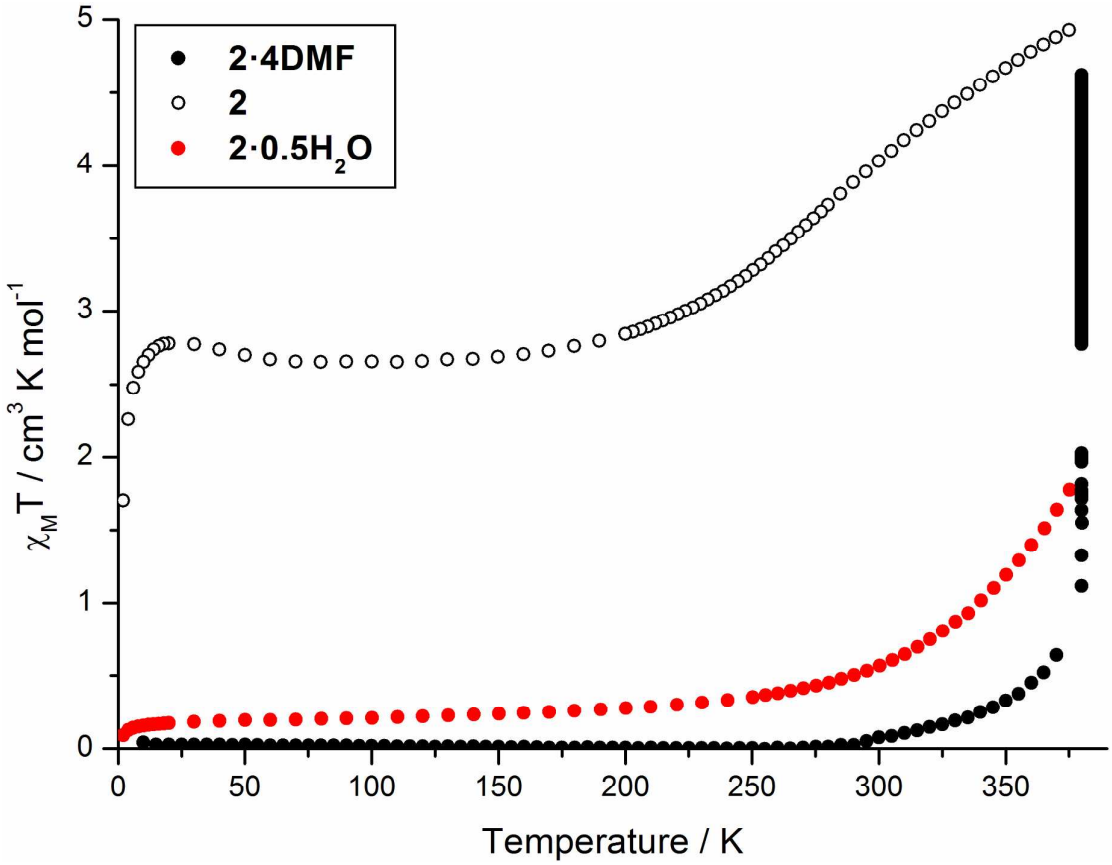

Figure S4: Overlay of the temperature dependence of $\chi_M T$ for compound **2·4DMF** ($[Fe_2(\mu\text{-}L)_2](ClO_4)_4$*4DMF), **2** ($[Fe_2(\mu\text{-}L)_2](ClO_4)_4$) and **2·0.5H$_2$O** ($[Fe_2(\mu\text{-}L)_2](ClO_4)_4$*0.5$H_2O$)[1].

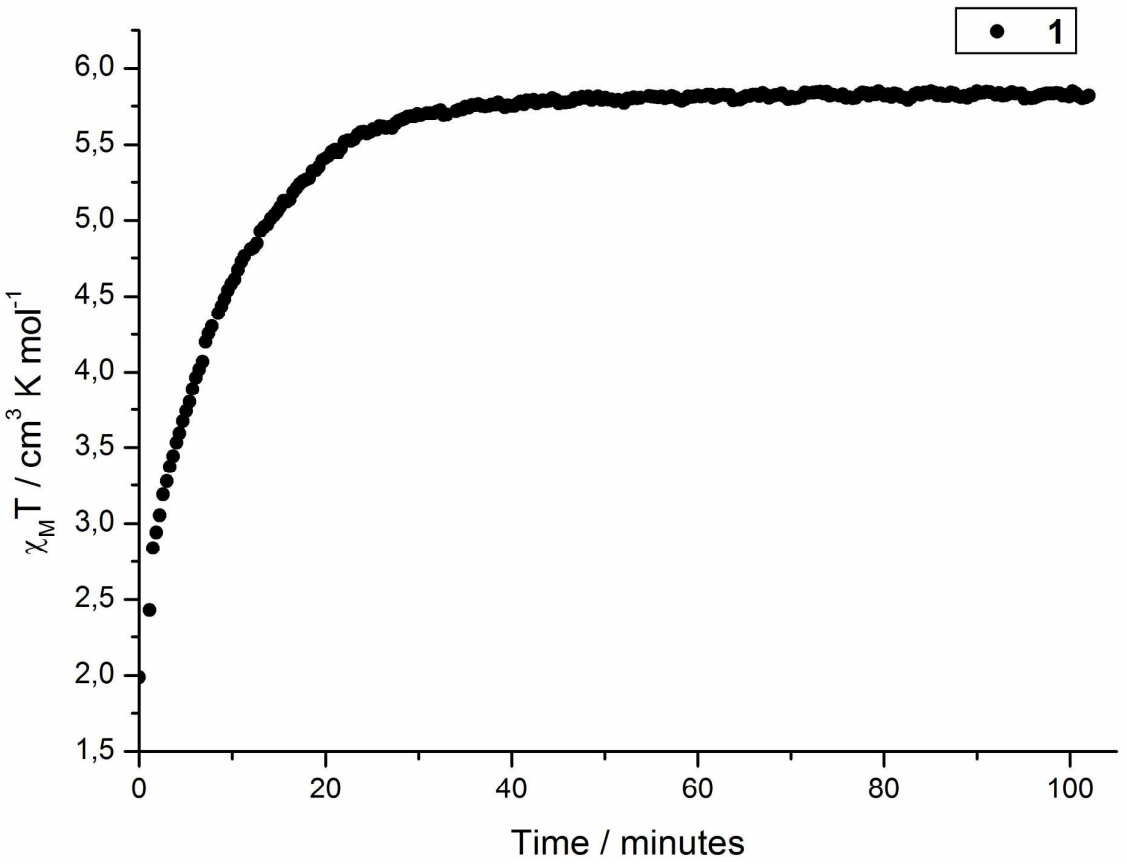

Figure S5: Time dependence of $\chi_M T$ at 380 K during the desolvation of **1·4DMF** ($[Fe_2(\mu\text{-}L)_2](BF_4)_4$*4DMF).

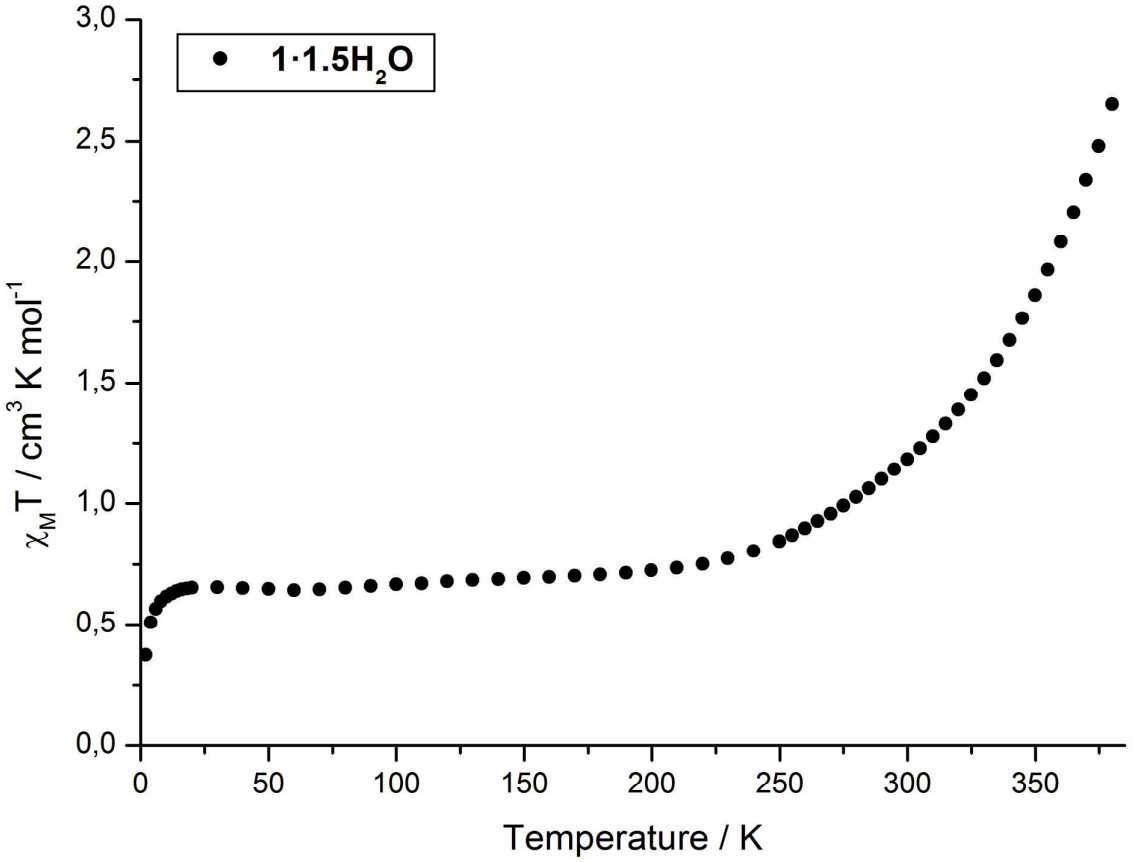

Figure S6: Temperature dependence of $\chi_M T$ for compound **1·1.5H$_2$O** ([Fe_2(μ-L)$_2$](BF_4)$_4$*1.5H_2O).

Mössbauer Spectroscopy

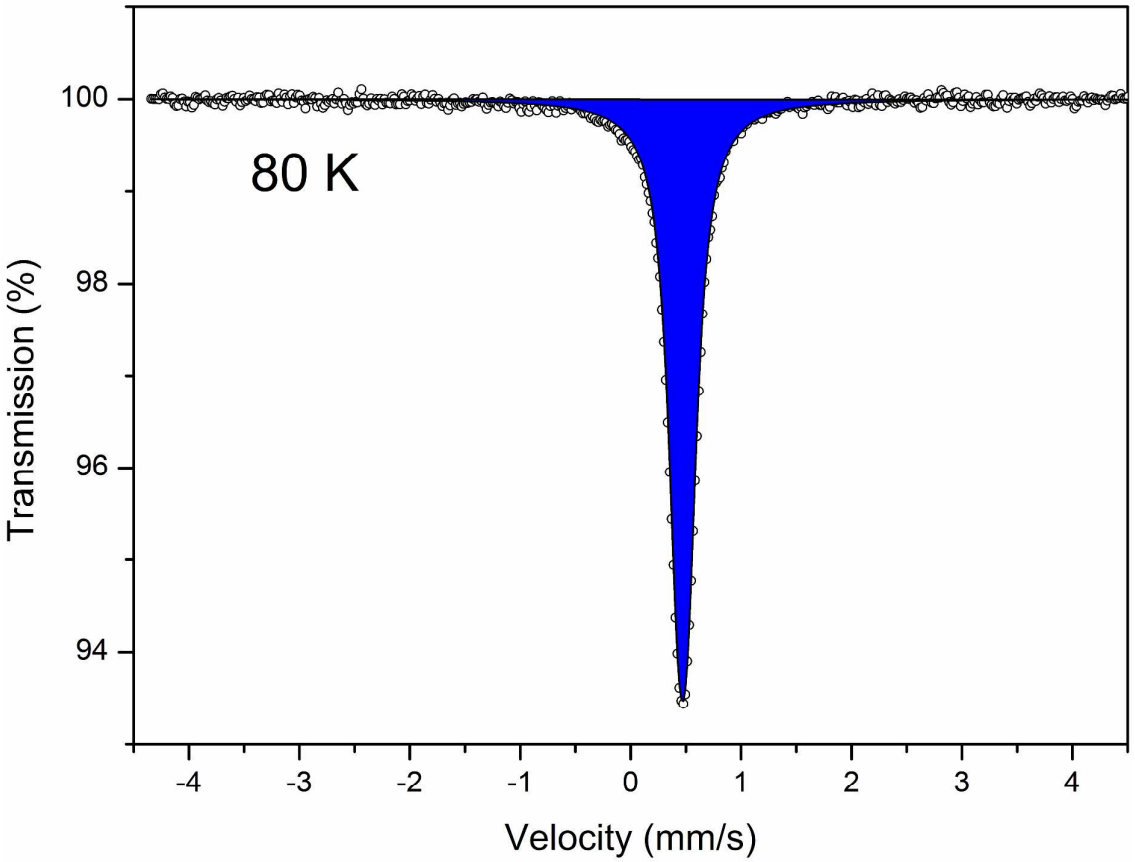

Figure S7: Mössbauer spectrum of compound **1·4DMF** ($[Fe_2(\mu\text{-}L)_2](BF_4)_4$*4DMF) at 80 K.

Table S4. Mössbauer parameters for compound **1·4DMF** at 80 K with the isomer shift δ, quadrupole splitting ΔE_Q, lorentzian line width Γ and site population.

Site Parameters			
	Isomer Shift δ (mm/s)	Quadrupole Splitting ΔE_Q (mm/s)	Lorentzian line width Γ (mm/s)
Doublet 1	0.47007	0.0857	0.1174
Compiled Site Properties			
	Site population (%)		
Doublet 1	100		

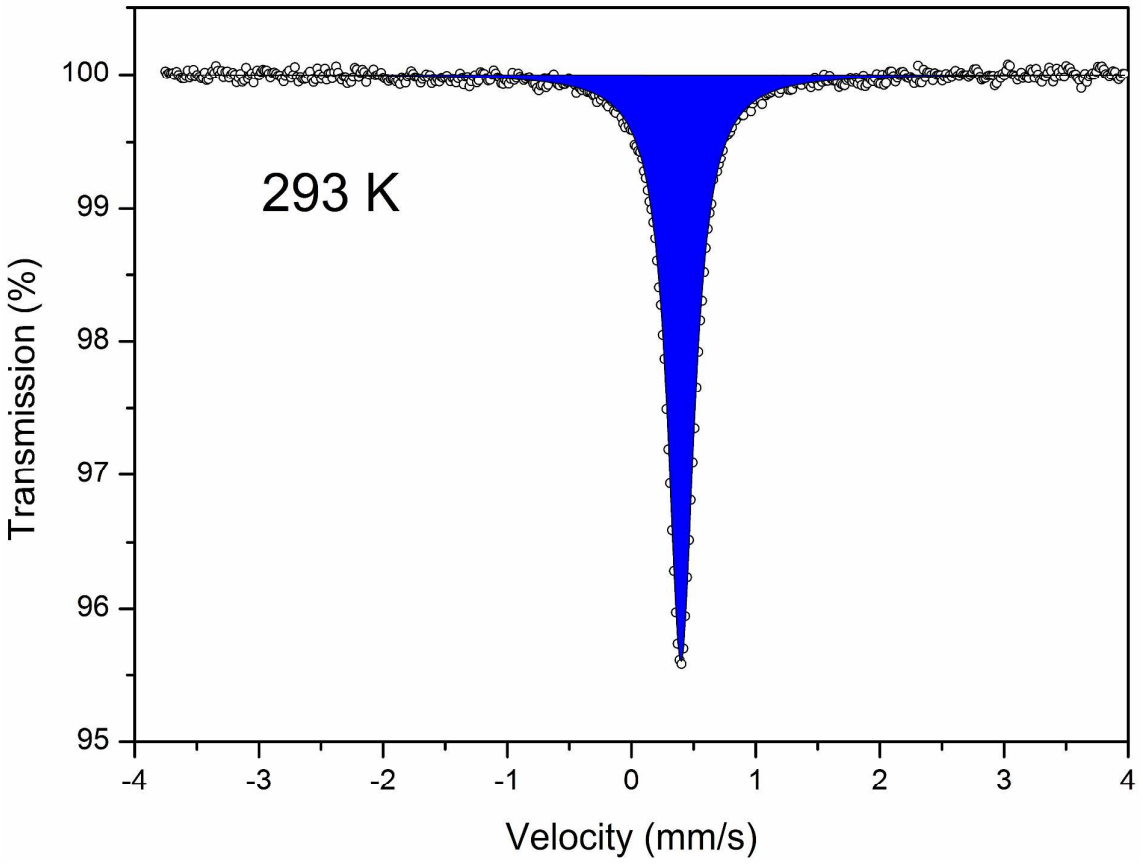

Figure S8: Mössbauer spectrum of compound **1·4DMF** ($[Fe_2(\mu\text{-}L)_2](BF_4)_4$*4DMF) at 293 K.

Table S5. Mössbauer parameters for compound **1·4DMF** at 293 K with the isomer shift δ, lorentzian line width Γ and site population.

Site Parameters		
	Isomer Shift δ (mm/s)	Lorentzian line width Γ (mm/s)
Singlet 1	0.3983	0.1308
Compiled Site Properties		
	Site population (%)	
Singlet 1	100	

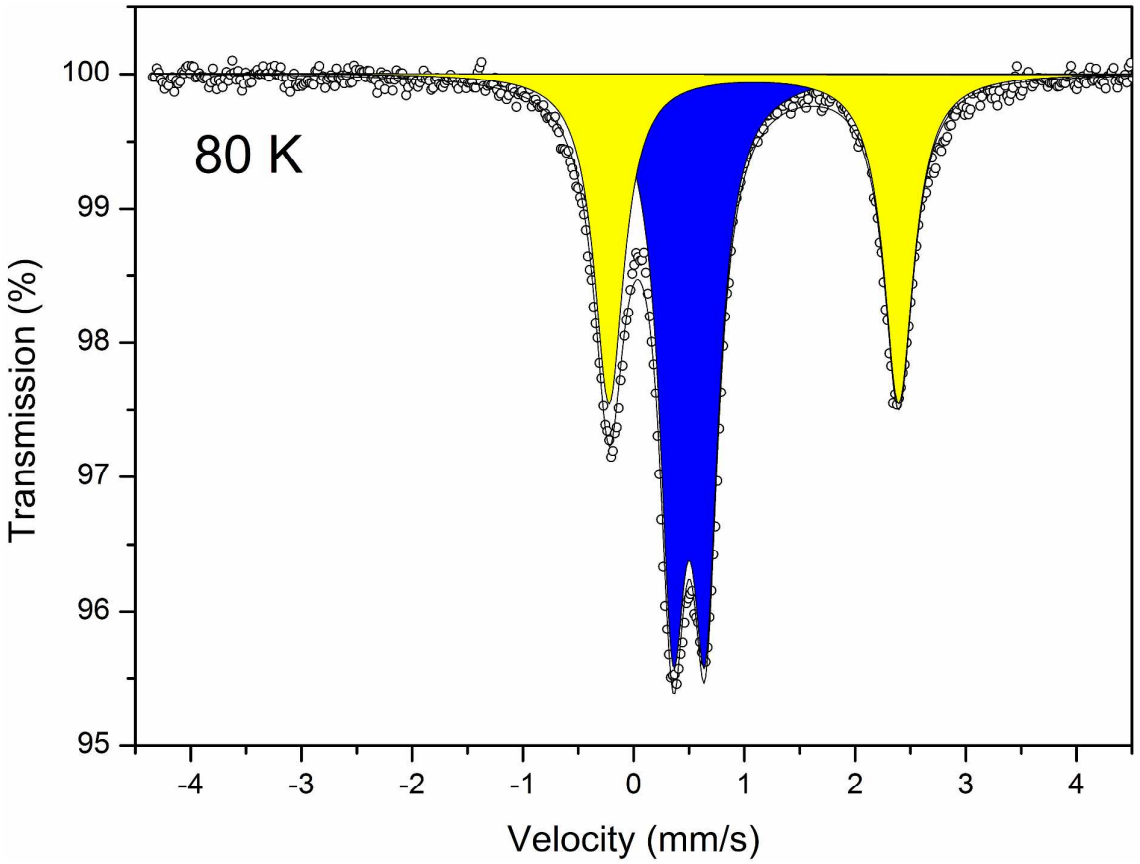

Figure S9: Mössbauer spectrum of compound **1** ($[Fe_2(\mu\text{-}L)_2](BF_4)_4$) at 80 K.

Table S6. Mössbauer parameters for compound **1** at 80 K with the isomer shift δ, quadrupole splitting ΔE_Q, lorentzian line width Γ and site population.

Site Parameters			
	Isomer Shift δ (mm/s)	Quadrupole Splitting ΔE_Q (mm/s)	Lorentzian line width Γ (mm/s)
Doublet 1	0.5005	0.2932	0.1438
Doublet 2	1.0856	2.6156	0.1638
Compiled Site Properties			
	Site population (%)		
Doublet 1	53.92		
Doublet 2	46.08		

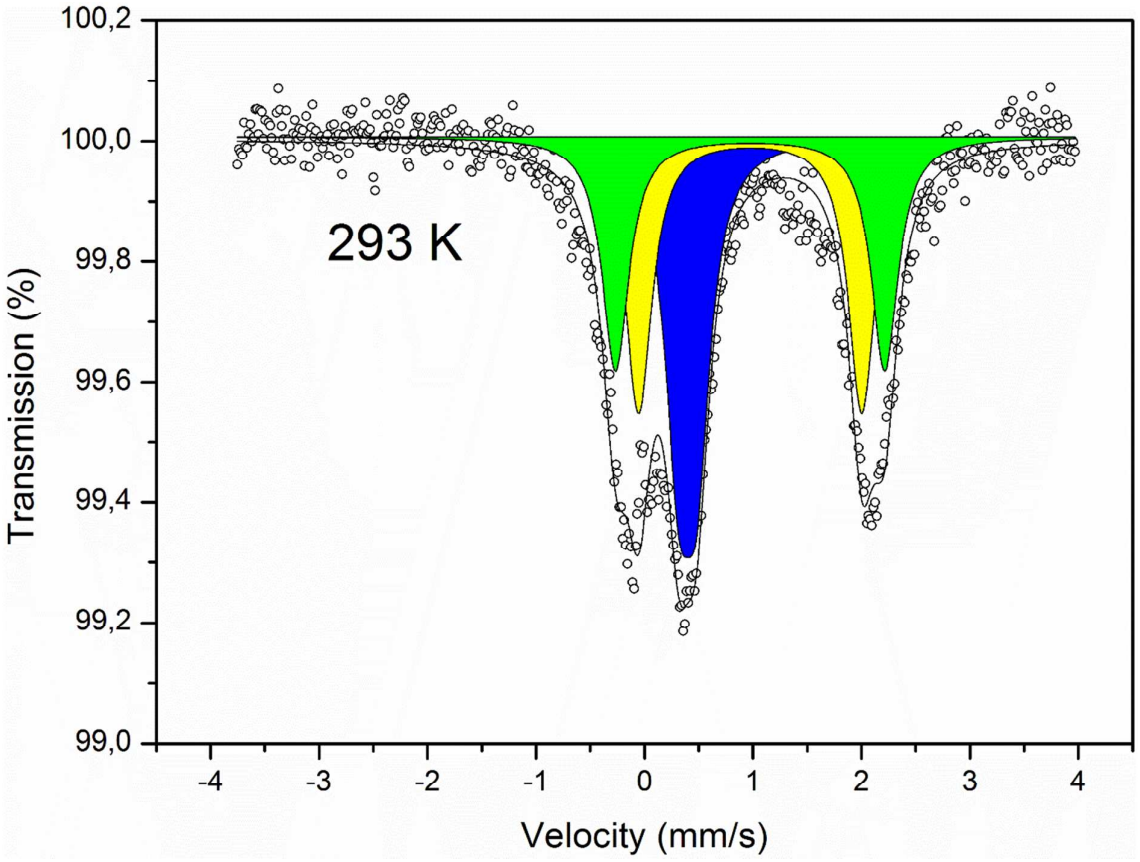

Figure S10: Mössbauer spectrum of compound **1** ($[Fe_2(\mu\text{-}L)_2](BF_4)_4$) at 293 K.

Table S7. Mössbauer parameters for compound **1** at 293 K with the isomer shift δ, quadrupole splitting ΔE_Q, lorentzian line width Γ and site population.

Site Parameters			
	Isomer Shift δ (mm/s)	Quadrupole Splitting ΔE_Q (mm/s)	Lorentzian line width Γ (mm/s)
Doublet 1	0.397	0.168	0.147
Doublet 2	0.974	2.057	0.15
Doublet 3	0.973	2.481	0.15
Compiled Site Properties			
	Site population (%)		
Doublet 1	35.2		
Doublet 2	35.1		
Doublet 3	29.7		

Infrared Spectroscopy

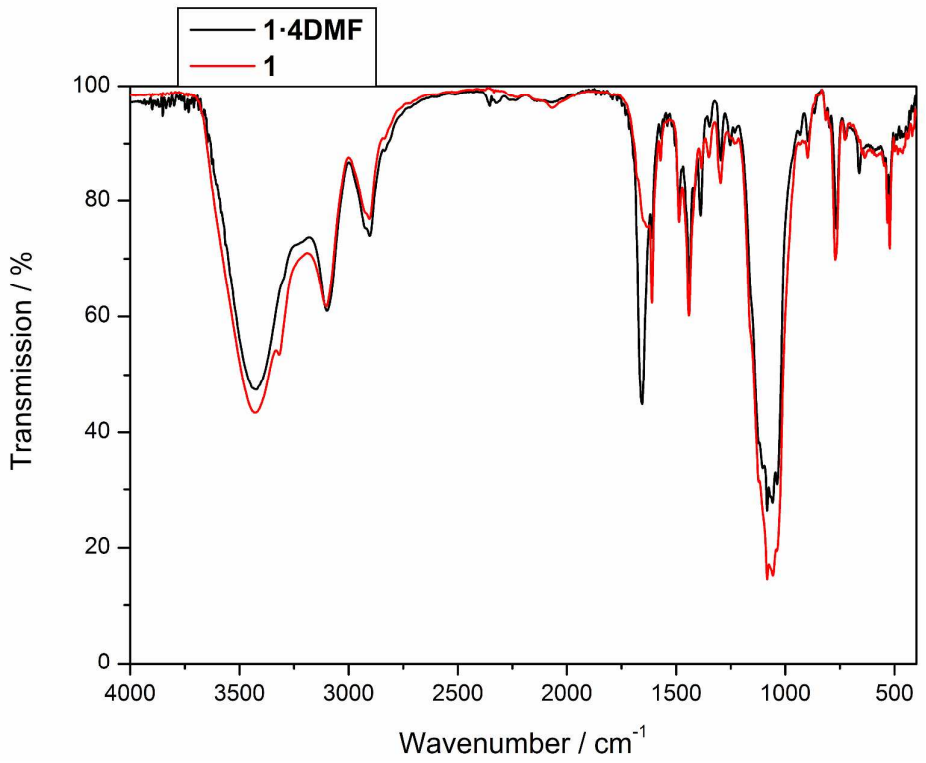

Figure S11: Overlay of the infrared spectra of compound **1·4DMF** ($[Fe_2(\mu\text{-}L)_2](BF_4)_4$*4DMF) and **1** ($[Fe_2(\mu\text{-}L)_2](BF_4)_4$).

The main difference in the infrared spectra of compound **1·4DMF** ($[Fe_2(\mu\text{-}L)_2](BF_4)_4$*4DMF) and **1** ($[Fe_2(\mu\text{-}L)_2](BF_4)_4$) are the absorption bands at 1656 cm^{-1}, 1388 cm^{-1} and 661 cm^{-1} which cannot be detected in the spectrum of the desolvated sample **1** or are at least extremely weak. The first absorption band (at 1656 cm^{-1}) in the spectrum of **1·4DMF** can be assigned to the ν(C=O) stretching vibration, the second band (at 1388 cm^{-1}) to the δ(CH) bending vibration and the third band (at 661 cm^{-1}) to the δ(C=O) bending vibration of the DMF in the single crystals and thus confirms the results of the elemental analysis and the loss of all four DMF molecules during the desolvation.[2, 3]

Furthermore, the ν(C=O) stretching vibration of the DMF is shifted to a lower wavenumber compared to the ν(C=O) stretching vibration of pure DMF, which appears at 1689 cm^{-1}.[2] This shift to lower energies is a sign for an elongated and weaker C=O bond, which is caused by the hydrogen bonding interactions to the secondary amines of the complex cation and the shift of electron density from the DMF oxygen atom towards the N-H of the ligand in the complex cation of **1·4DMF**.

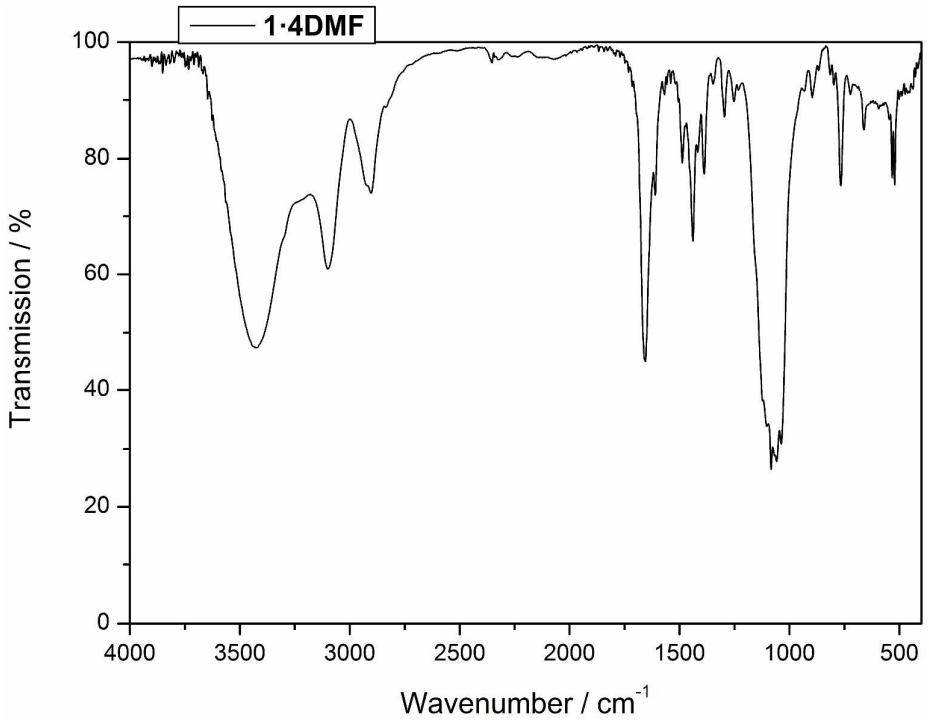

Figure S12: Infrared spectrum of compound **1·4DMF** ($[Fe_2(\mu\text{-}L)_2](BF_4)_4$*4DMF).

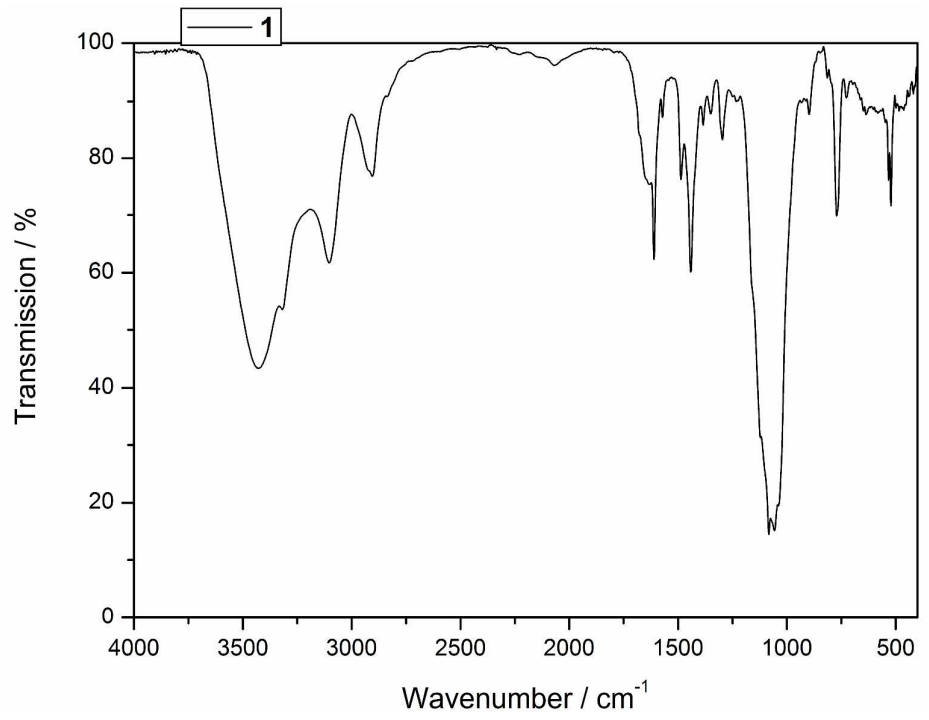

Figure S13: Infrared spectrum of compound **1** ($[Fe_2(\mu\text{-}L)_2](BF_4)_4$).

The IR spectra of the complexes after each cycling process (Figures S12 and S13) clearly show the presence of bound DMF after the resolvation processes. The v(C=O) stretching vibration of DMF around 1656 cm^{-1} can be used as a tensor to monitor the DMF uptake and release during the desolvation and resolvation process. The IR spectra in Figure S12 all show a strong absorption band for the v(C=O) stretching vibration of DMF with the shift to lower wavenumbers confirming the hydrogen bonding interactions between the DMF and the complexes, as explained above. The v(C=O) stretching vibration cannot be detected in the IR spectra after the desolvation at 150 °C under high vacuum (Figure S13). This confirms that DMF is removed from the sample during the desolvation process.

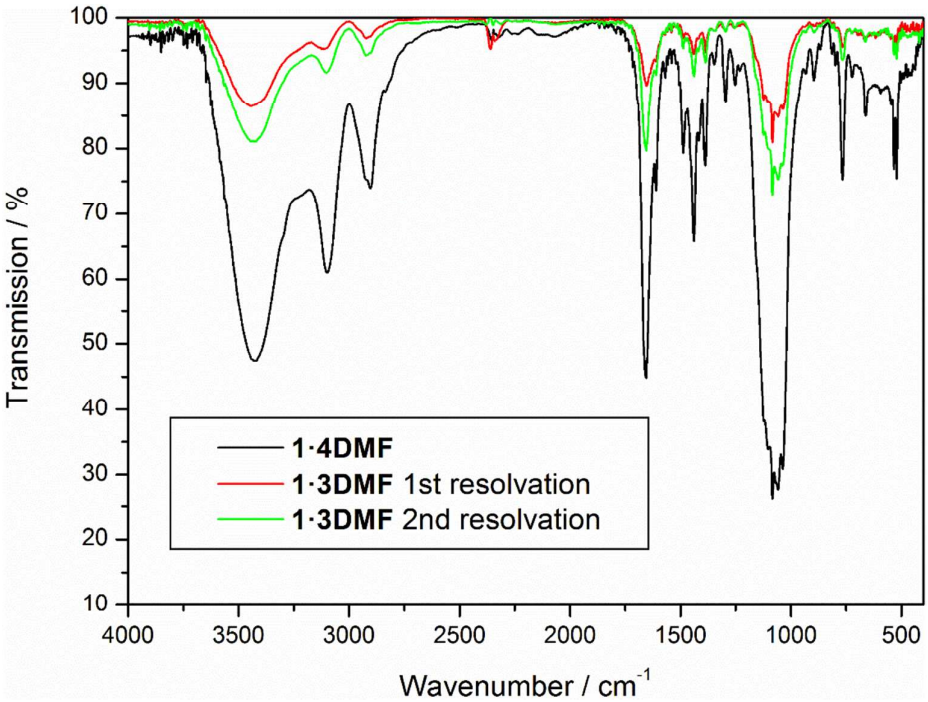

Figure S14: Infrared spectra of compound **1·4DMF** before the first desolvation and **1·3DMF** after each resolvation.

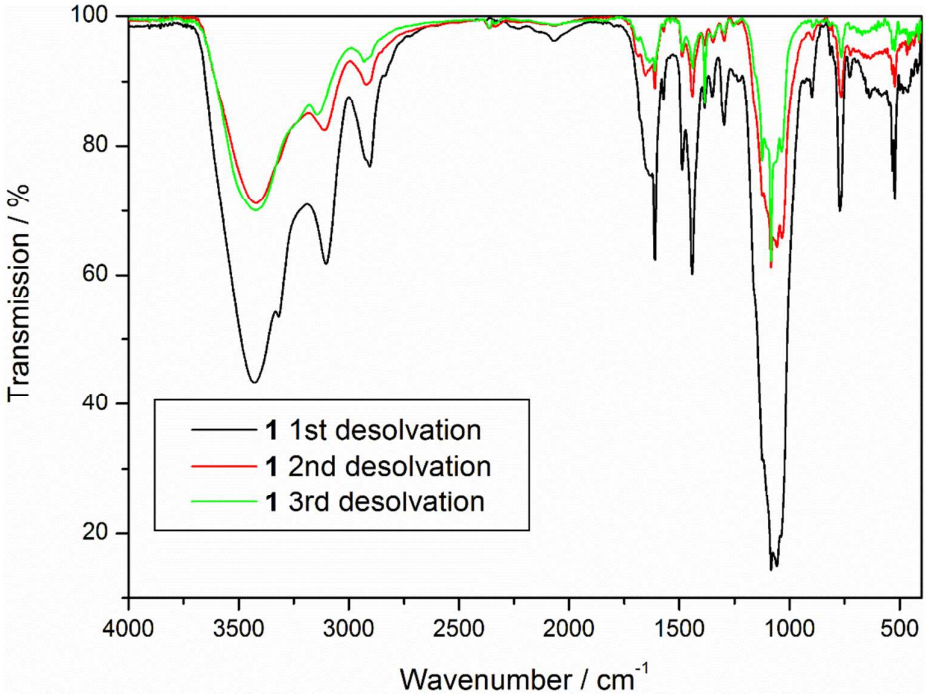

Figure S15: Infrared spectrum of compound **1** ($[Fe_2(\mu\text{-}L)_2](BF_4)_4$) after each desolvation.

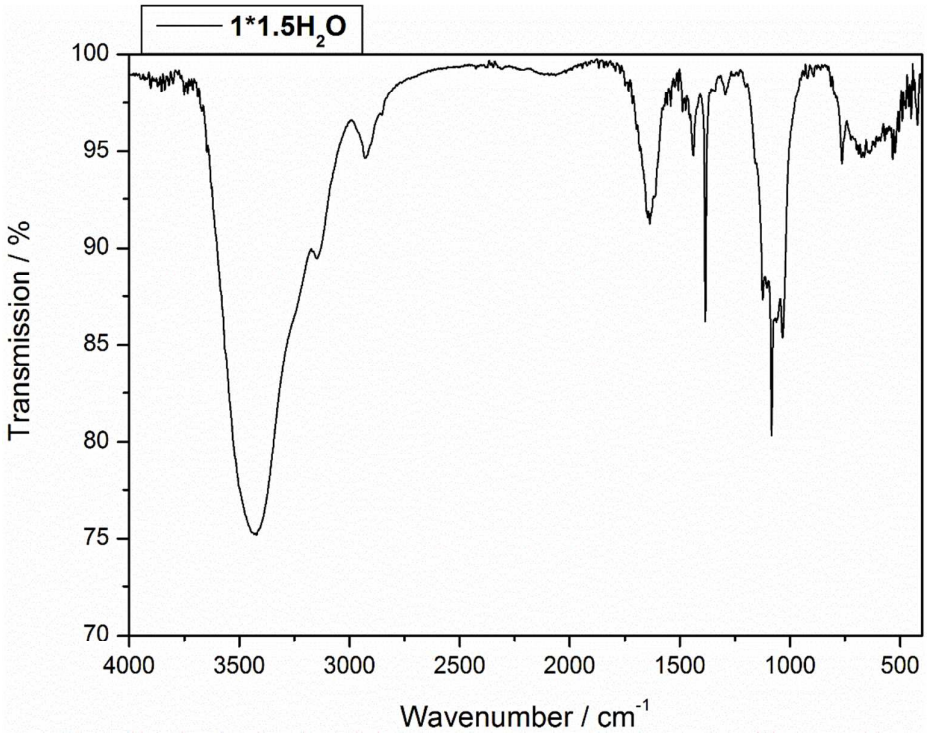

Figure S16: Infrared spectrum of compound **1·1.5H$_2$O** ($[Fe_2(\mu\text{-}L)_2](BF_4)_4$*1.5$H_2O$).

The difference in the IR spectra of **1** (after desolvation, Figure S11) and **1·1.5H$_2$O** (after the hydration of **1**, Figure S14) can be seen in the absorption bands at 3422 cm^{-1} and 1636 cm^{-1}, with the first being assigned to the stretching vibrations and the second to the deformation vibrations of water.[4]

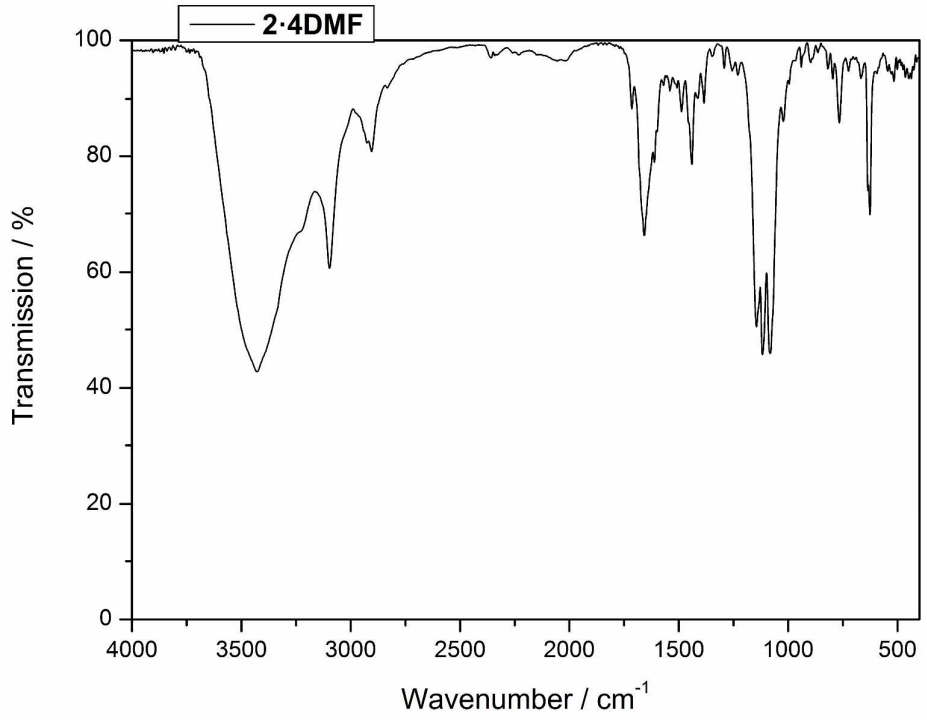

Figure S17: Infrared spectrum of compound **2·4DMF** ([Fe_2(μ-L)$_2$](ClO_4)$_4$*4DMF).

Thermogravimetric analysis

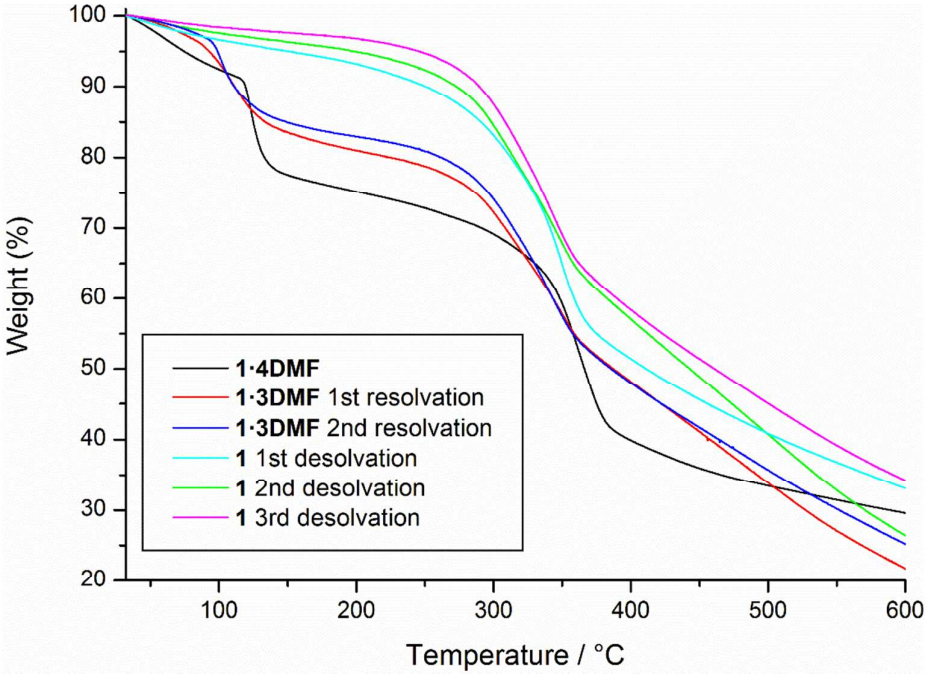

Figure S18: TGA of compound **1·4DMF/1·3DMF** and **1** after the desolvation and resolvation cycles.

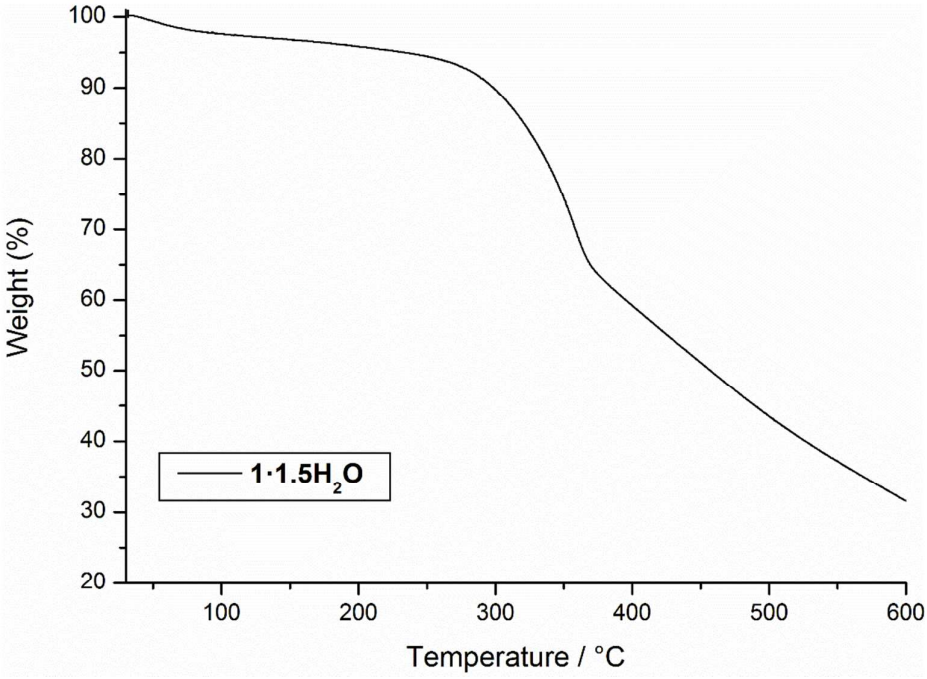

Figure S19: TGA of compound **1·1.5H_2O** ($[Fe_2(\mu\text{-}L)_2](BF_4)_4$*1.5$H_2O$).

References

1. Herold, C. F.; Carrella, L. M.; Rentschler, E., *Eur. J. Inorg. Chem.* **2015**, 3632-3636.
2. M.B. Shundalau, P. S. C., A.I. Komyak,A.P. Zazhogin,M.A. Ksenofontov,D.S. Umreiko, *J. Appl. Spectrosc.* **2011,** *78*.
3. Lumley Jones, R., *J. Mol. Spectrosc.* **1963,** *11*, 411-421.
4. Max, J. J.; Chapados, C., *J. Chem. Phys.* **2009,** *131*, 184505.